Icarus 359 (2021) 114327

Contents lists available at ScienceDirect

Icarus

journal homepage: www.elsevier.com/locate/icarus

Geochemistry of the Von Kármán crater floor and thickness of the non-mare ejecta over the Chang'e-4 landing area

Dijun Guo [a,*], Wenzhe Fa [a,b,c], Xiaojia Zeng [d], Jun Du [a], Jianzhong Liu [d,c]

[a] Institute of Remote Sensing and Geographical Information System, School of Earth and Space Sciences, Peking University, Beijing, China
[b] State Key Laboratory of Lunar and Planetary Sciences, Macau University of Science and Technology, Macau, China
[c] CAS Center for Excellence in Comparative Planetology, Hefei, China
[d] Center for Lunar and Planetary Sciences, Institute of Geochemistry, Chinese Academy of Sciences, Guiyang, China

ARTICLE INFO

Keywords:
Moon
Chang'e-4
Von Kármán crater
Ejecta deposits
Dark-haloed crater

ABSTRACT

China's Chang'e-4 mission has carried out the first ever lunar farside landing exploration on the floor of the Von Kármán crater, a geologically complex region located in the most ancient and deepest South Pole-Aitken (SPA) basin. In order to demonstrate the characteristics of materials in the landing area, we investigated the regional geochemistry and thickness of non-mare ejecta overlaying the mare basalts. Comparative analyses of FeO, TiO_2 and Th concentrations suggest that the landing site surface is dominated by non-mare ejecta from nearby craters (e.g., Finsen crater) with part of basaltic materials. The ejecta thickness is estimated based on the excavation depth of dark-haloed and non-dark-haloed craters by using support-vector machine, a supervised machine learning method for classification. The results show that the ejecta thickness in the region of 40 km across the landing site varies from near zero to ~80 m with a mean value of ~41 m. The ejecta at the Chang'e-4 landing site is ~40 m thick, which is comparable to the in situ observations by the Lunar Penetrating Radar onboard the Yutu-2 rover. Our results provide valuable information for interpretation of the on-going returned data and geologic analysis of the Chang'e-4 exploration region.

1. Introduction

1.1. Geologic context

The Earth's Moon is characterized by its asymmetry of the nearside and the farside (e.g., Wieczorek et al., 2013). Since the 1960s, the nearside has been visited more than 10 times during previous landed missions, based on which, fundamental concepts of lunar science have been established. On the other hand, the farside has remained as an untouched territory until 3 January 2019, the lander of China's Chang'e-4 (CE-4) probe touched down at the Statio Tianhe (177.5991°E, 45.4446°S) in the southern floor of the Von Kármán crater (~186 km in diameter) (Fig. 1; Li et al., 2019). Assembled with instruments including Panoramic Camera (PCAM), Visible and Near Infrared Spectrometer (VNIS) and Lunar Penetrating Radar (LPR) (Di et al., 2019; Li et al., 2019; Li et al., 2020), the CE-4 mission provides an unprecedented opportunity to investigate the Moon's farside. The mission is anticipated to improve our knowledge of the composition, subsurface structure and geologic evolution of the unique South Pole-Aitken (SPA) terrane (Jia et al., 2018; Jolliff et al., 2000).

The exploration target (the Von Kármán crater), was carefully chosen to be inside the giant SPA basin, one of the Moon's most scientifically rich regions (e.g., Jolliff et al., 2017). About 2400 km in diameter (Garrick-Bethell and Zuber, 2009), the SPA basin is the largest impact depression on the Moon and is thought to be formed from an impact that penetrated through the ancient lunar crust and excavated the mantle materials whose composition is highly debatable (e.g., Charlier et al., 2018; Elkins-Tanton et al., 2011). As the oldest impact basin on the Moon, the SPA basin was formed ~4.2–4.3 Ga based on crater statistics (Garrick-Bethell et al., 2020; Orgel et al., 2018), which might correspond to the termination of the magma ocean solidification (Elkins-Tanton et al., 2011). In such a scenario, the SPA impact excavated the primordial lunar crust that was in special thermal condition compared with the subsequent great impacts. Considering the extremely large scale, the SPA basin could produce significant volume of impact melts that might undergo differentiation (e.g., Uemoto et al., 2017; Vaughan and Head, 2014). Exploring at the surface of the interior SPA basin, the scientific data returned from the CE-4 mission are critical for

* Corresponding author.
E-mail address: djguo@pku.edu.cn (D. Guo).

https://doi.org/10.1016/j.icarus.2021.114327
Received 14 October 2020; Received in revised form 16 December 2020; Accepted 14 January 2021
Available online 21 January 2021

deciphering the formation and evolution of the SPA basin.

As shown in Fig. 1b, the floor of the Von Kármán crater is ~ − 6 km in elevation. Based on the Gravity Recovery and Interior Laboratory (GRAIL) data, the crustal thickness in the Von Kármán region is estimated to be less than 10 km (Wieczorek et al., 2013). Scaling law suggests that a crater of 180 km diameter can excavate 12 km in depth (Melosh, 1989), thus it is conceivable that the Von Kármán crater could expose materials from the lower crust or the upper mantle. The model age of the Von Kármán crater is ~4.2 Ga (Lu et al., 2021), and the floor of this Pre-Nectarian crater was flooded by mare basalts during Imbrian period (~3.2 Ga) (Lu et al., 2021), resulting in flat topography (Fig. 1b) and low albedo (Fig. 1c). After emplaced, large areas of the mare have been modified and covered by feldspathic materials that appear brighter than mare basalts (Fig. 1c). As shown in Fig. 1d, the bright materials are distributed with secondary impacting linear features on the surface, indicating that the ejecta approached from the northeast and that the parent crater could be the Eratosthenian-aged Finsen crater (~73 km in diameter) (Di et al., 2019; Huang et al., 2018; Lu et al., 2021). Young craters that are large enough to penetrate through the ejecta deposits can excavate substratum low-albedo mare basalts (Supplementary Fig. 1a), appearing as dark-haloed craters (DHCs) (Antonenko et al., 1995; Bell and Hawke, 1984). Such craters can be used to estimate the

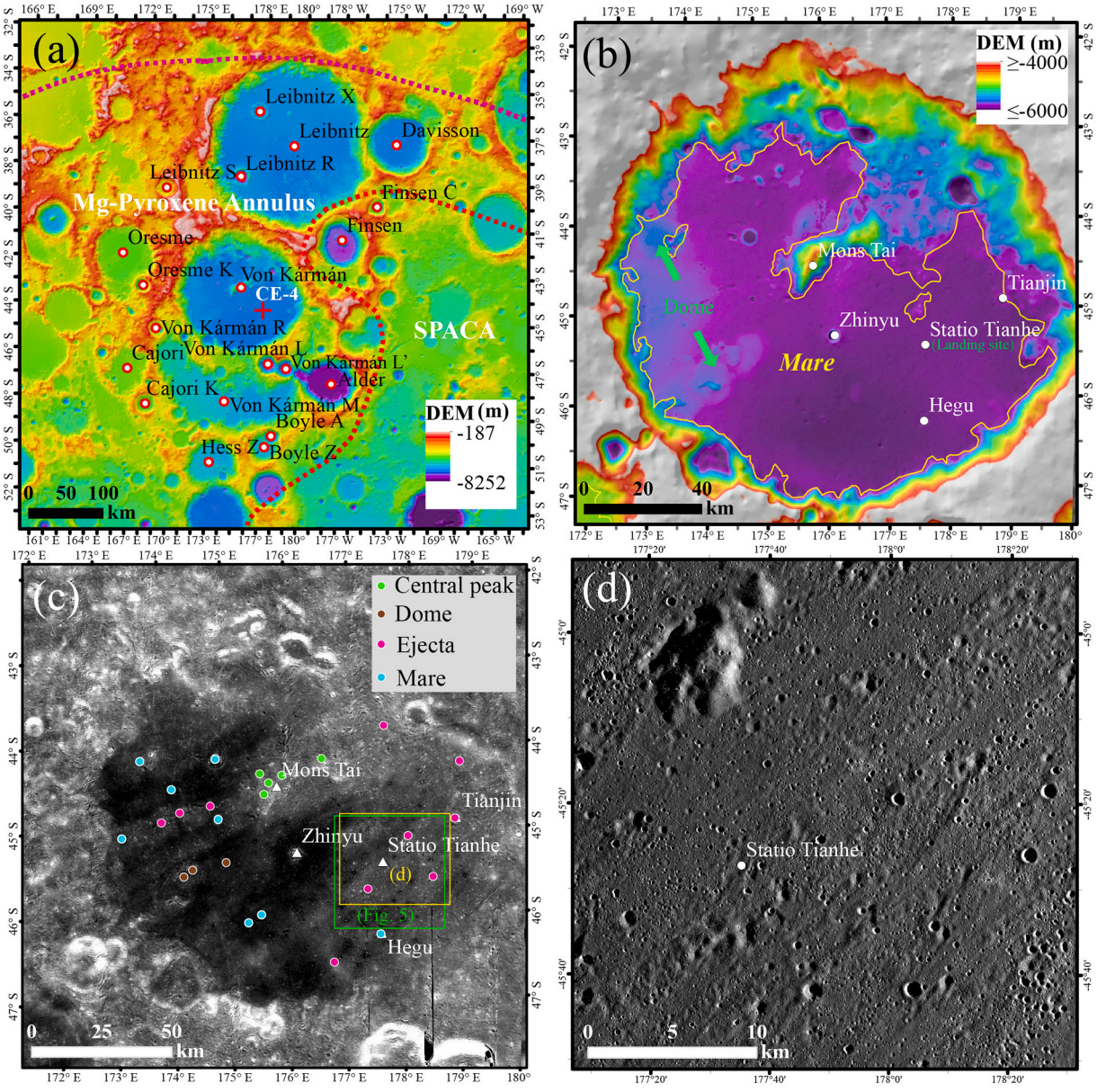

Fig. 1. (a) Topography and geologic features around the Von Kármán crater. SPA compositional anomaly (SPACA) and Mg-Pyroxene represent the annuli containing elevated Ca, Fe-rich pyroxene and Mg-pyroxene, respectively (Moriarty and Pieters, 2018). Von Kármán L' is an unofficially named crater given by Huang et al. (2018). (b) Topography of the interior of the Von Kármán crater. The yellow line represents the boundary of mare basalts identified from Lunar Reconnaissance Orbiter Camera (LROC) images (Nelson et al., 2014). White dots designate the new nomenclatures accepted by IAU after the landing of the CE-4 mission, where Statio Tianhe is the CE-4 landing site and Mons Tai is the central peak of the Von Kármán crater. Two dome-like features are marked with green arrows. The elevation is obtained from SELENE and LRO DEM 2015 (SLDEM2015) (Barker et al., 2016). (c) Kaguya Multiband Imager (MI) 1000 nm band image. The dots represent locations of different geologic units for geochemical data extraction in Section 2.2. Green square in (c) marks the extent of Fig. 5 where the DHCs and non-DHCs are identified. Yellow square in (c) marks the extent of (d), which shows the linear features from northeast to southwest in Kaguya Terrain Camera (TC) images (~7.4 m/pixel). Based on the texture and alignment, the linear features may represent the ejecta deposits from Finsen crater. (For interpretation of the references to colour in this figure legend, the reader is referred to the web version of this article.)

thickness of the non-mare ejecta emplaced above mare basalts, which will be discussed in Section 3.

1.2. Motivation of this study

On the surface of the Von Kármán floor, the composition is nonuniform due to modifications of subsequent evolution processes: eruption of the mare basalts, emplacements of extraneous non-mare ejecta, mixture through local cratering events (Huang et al., 2018). Compositional signatures of the material and thickness of accumulated extraneous ejecta are key information to understand the geologic evolution and interpret the data returned from the CE-4 mission. At the CE-4 landing site, the albedo is obviously higher than mare basalts (Fig. 1c) while their optical maturity (OMAT) does not show any significant variations (Fig. 2), indicating that feldspathic component is rich in materials of the landing site as suggested by previous studies (e.g., Gou et al., 2019; Lin et al., 2019). Ejecta deposits are also evident from the linear features where the CE-4 is landed (Fig. 1d). However, it is debated about the origin of regolith minerals. Initial analysis of the CE-4 VNIS spectroscopic data suggests that the regolith at the landing region is rich in low-calcium pyroxene (LCP) and olivine that originated from the mantle (Li et al., 2019), which is supported by Gou et al. (2019). However, other studies argued that the materials were originated from impact melt crystallization inside the SPA basin based on their enriched plagioclase (Hu et al., 2019; Lin et al., 2019). Remote sensing investigation of surface compositions over a wide area is critical for unveiling the sources of the materials. Several studies have estimated the thickness of extraneous ejecta at the landing site using different approaches and data (e.g., Di et al., 2019; Huang et al., 2018; Lai et al., 2019; Li et al., 2020), but their results are inconsistent and vary from ~30 m to more than 70 m. Using ejecta thickness decay models, Huang et al. (2018) estimated that the thickness at the landing area is ~7.2–15.5 m. However, this model prediction is not supported by direct measurements. Based on the CE-4 LPR observations, Lai et al. (2019) proposed that the ejecta thickness is ~26 m by assuming that the real parts of the dielectric permittivity values before and after 154 ns are 4.3 and 6, respectively. Through topographic difference and impact cratering simulations of Finsen and Alder craters, Di et al. (2019) suggested that the thickness of ejecta from these two craters accumulated to ~70 m at the CE-4 landing site. But the ejecta thickness model was not tested through observations of craters at comparative scale, and the study area is located in the discontinuous ejecta field where the thickness could vary substantially. Using LPR data of the first two lunar days, Li et al. (2020) reported that the ejecta are ~40 m thick at the landing site, which is in the range of depth estimated from DHCs and non-DHCs. However, their estimation has a wide range from 34 m to 78 m, and therefore the constraint to the radar observations is weak. To get reliable results, the in situ radar detections should be well constrained by geological evidences.

With a systematic study of compositions and sources of surface

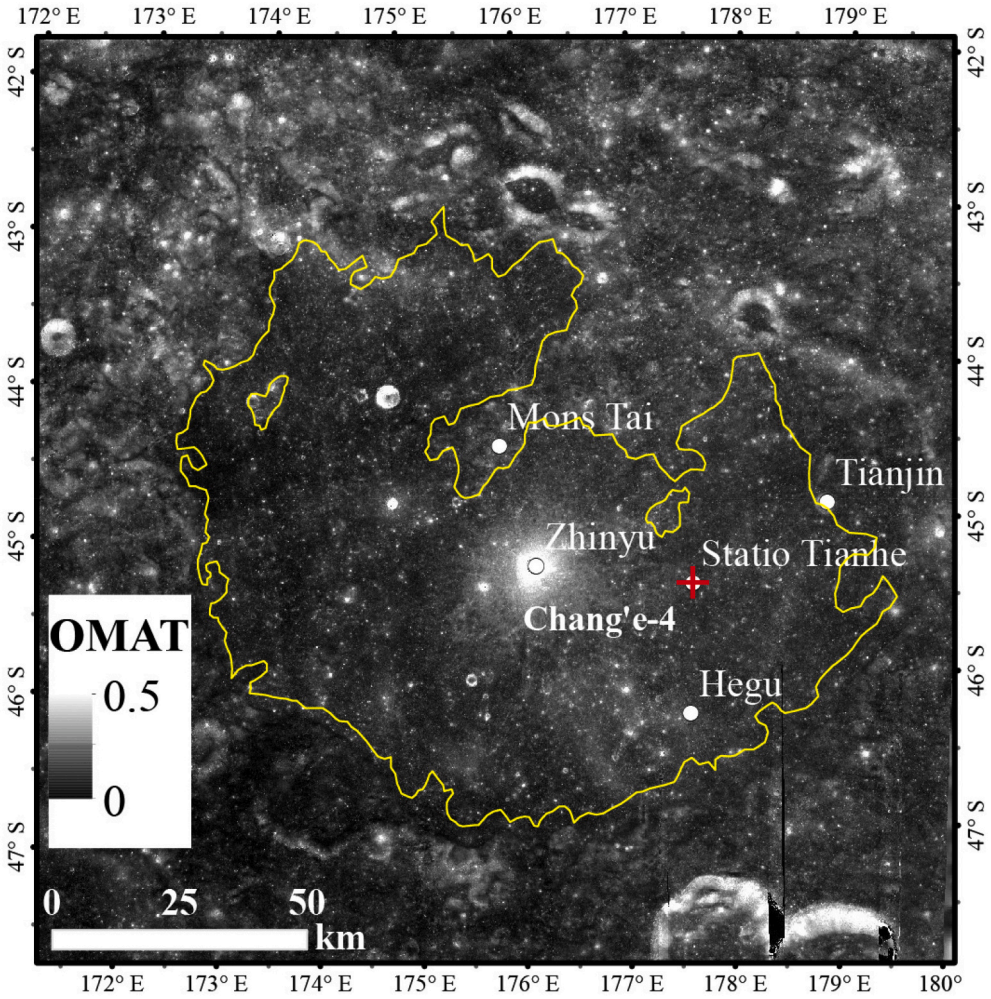

Fig. 2. OMAT of the Von Kármán crater derived from MI data using the method in Lemelin et al. (2016). The yellow line represents the boundary of mare basalts in Fig. 1b. The CE-4 landing site is marked by the red cross at the Statio Tianhe. (For interpretation of the references to colour in this figure legend, the reader is referred to the web version of this article.)

materials in the CE-4 landing area, new results can be used to resolve the controversial results in the aforementioned studies. The VNIS is able to detect the surface compositions, but the observation targets are limited on the traverse trail. By combining the geologic context, geochemical analysis (especially TiO_2, FeO and Th distribution) in a broader view is an important complement to interpret the data and analyze the geologic processes and evolution of the exploration region. TiO_2 and FeO concentrations are essential to estimate the complex dielectric permittivity, which is critical in processing the LPR data (Fa and Wieczorek, 2012). On the other hand, even though the LPR can reflect the subsurface structures, additional geologic information is necessary in interpreting the observed radargram. Overlaying on the mare basalts, the non-mare ejecta are the most important component of local regolith and their thickness range is a key prior knowledge for LPR data interpretation. Properties of ejecta deposits are also fundamental in understanding cratering process and lunar surface evolution. This work carries out comparative analysis of the geochemistry in different units of the Von Kármán crater, which is used to analyze the compositional characteristics and evolution history in the landing area (Section 2). By employing both DHCs and non-DHCs on the Von Kármán crater floor, we proposed an innovative method to estimate the regional thickness of accumulated non-mare ejecta above mare basalts (Section 3). The ejecta thickness

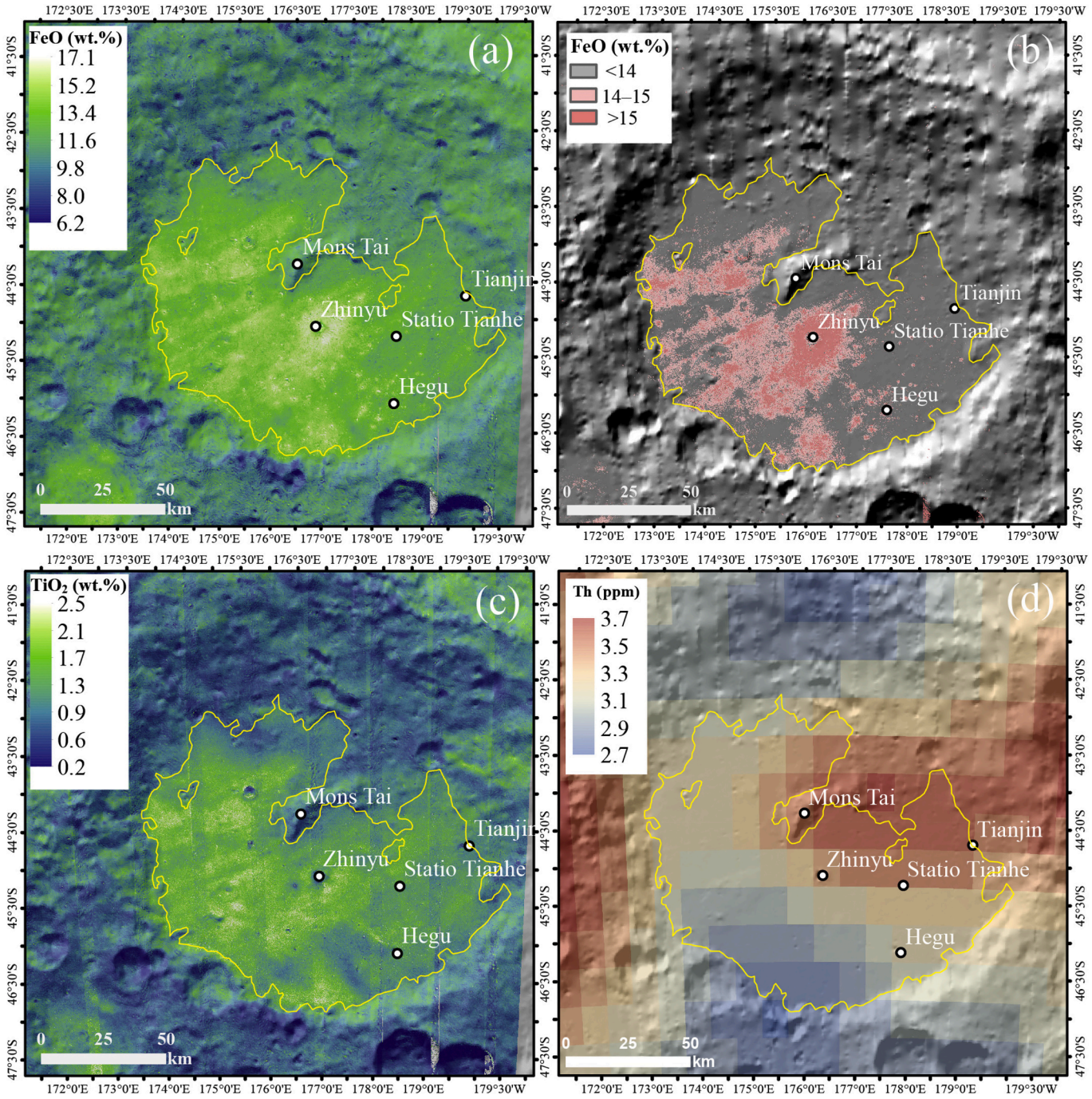

Fig. 3. (a), (c) and (d) are FeO, TiO_2 and Th concentrations of the Von Kármán crater; (b) shows the three FeO concentration groups. The yellow line represents the boundary of mare basalts as Fig. 1b. The standard deviation of TiO_2 concentration is 0.43 wt.% (Otake et al., 2012); the root-mean-square error of FeO concentration is 1 wt.% (Lemelin et al., 2015). The uncertainty of the thorium concentration is <0.5 ppm (Lawrence et al., 2002; Lawrence et al., 2000). (For interpretation of the references to colour in this figure legend, the reader is referred to the web version of this article.)

results are compared with the CE-4 LPR in situ measurements in Section 4. In Section 5, we discussed the ejecta thickness at the CE-4 landing site, the possible ejecta sources, and the regional evolution.

2. Geochemistry in the Von Kármán crater floor

Remote sensing observations and sample analyses reveal that lunar surface materials show diverse chemical compositions in FeO and Th concentrations (e.g., Korotev, 2005): the feldspathic-rich highland materials are characterized by relatively low concentrations of FeO and Th; basaltic rocks are mafic-rich with relatively high concentration of FeO and low concentration of Th; and the KREEP-rich samples are distinctly rich in Th (i.e., >4 ppm). This indicates that the FeO and Th concentrations could be used to distinguish different lithologies on the Moon. As mare basalts exhibit a wide range of TiO_2 concentration (i.e., from <1 wt.% to up to >14 wt.%; Neal and Taylor, 1992), different types of lunar basaltic lithologies can be well distinguished by comparing the FeO and TiO_2 contents. In the case of surface materials at the Von Kármán crater, their chemical features (i.e., FeO, TiO_2 and Th) can help us to understand the types and characteristics of regolith in this area. This study used multiple datasets to address the chemical composition of the Von Kármán region and the CE-4 landing site. Kaguya Multiband Imager (MI) data (~20 m/pixel) are used to derive the FeO and TiO_2 concentrations based on the algorithms in Lemelin et al. (2015) and Otake et al. (2012), respectively. Comparing with other multispectral data such as Clementine Ultraviolet/Visible camera (UVVIS) and LRO Wide Angle Camera (WAC) data, MI data have a higher spatial resolution and a good coverage. The algorithms have a standard deviations of 0.43 wt.% for TiO_2 and a root-mean-square error of 1 wt.% for FeO (Lemelin et al., 2015; Otake et al., 2012). The Th concentration is obtained from the Lunar Prospector (LP) Gamma Ray Spectrometer (GRS) data with a spatial resolution of 0.5°/pixel and an uncertainty of 0.5 ppm (Lawrence et al., 2002).

2.1. Overall distribution

Fig. 3 shows the FeO, TiO_2 and Th concentrations of the Von Kármán crater. It can be seen that iron and titanium contents are higher on the floor than those of the wall and exterior parts, and their distributions are spatially highly inhomogeneous (Fig. 3). Measurements of lunar samples show that mare basalts have Th concentration of ~0.2–3.2 ppm and FeO concentration of ~16–23 wt.% (Lucey et al., 2006). To address the possible occurrences of the purest mare basalts on the Von Kármán floor and assess the basaltic materials at the CE-4 landing region, the FeO concentration is divided into three groups: the high-FeO group, the intermediate-FeO group, and the low-FeO group (Fig. 3b). The high-FeO group represents the purest basalts in the investigation region. Considering the uncertainty in the FeO calculation algorithm (Lemelin et al., 2015), the threshold of the high-FeO group is 15 wt.% (Fig. 3b). The low-FeO group represents the regions where the composition is dominated by non-mare ejecta transported from craters outside of the Von Kármán. Their FeO concentrations are generally less than 14 wt.% (Fig. 3b). The group of intermediate FeO is 14–15 wt.% in concentration, which generally encompasses the high-FeO units (Fig. 3b) and could represent high-FeO margins that are slightly contaminated by non-mare materials. Based on Fig. 3b, the purest mare basalts cover very limited regions of the Von Kármán floor and the largest patch of the high-FeO unit is around the Zhinyu crater (176.15°E, 45.34°S). With a rim diameter of ~3.8 km, Zhinyu crater could excavate to the maximum depth of ~320 m based on scaling laws (Melosh, 1989). However, the FeO and TiO_2 concentrations of the ejecta near the Zhinyu crater rim where the materials are from the deepest region are relatively lower than those of the Zhinyu ejecta that deposited in further distance (Fig. 3a-c). It indicates that Zhinyu crater penetrated through the basaltic layer and excavated the pre-mare substrate, therefore the local mare basalts can not extend to more than 320 m in depth. The TiO_2 concentration of mare basalts on the Von Kármán crater floor is less than 2.5 wt.% (Fig. 3c and Fig. 4b) and belongs to low-titanium basalts (Lucey et al., 2006). Th is enhanced in the east crater floor where more ejecta from Finsen crater were emplaced. Garrick-Bethell and Zuber (2005) suggests the Th anomaly in the SPA basin is an indigenous unit and likely emplaced when the basin was formed. Some other studies ascribe the Th-enriched material to the antipodal ejecta convergence of Imbrium or Serenitatis basin (Haskin et al., 2004; Wieczorek and Zuber, 2001).

2.2. Geochemistry in different units

The latest geologic maps show that the floor of the Von Kármán crater consists of several individual geologic units (Fortezzo et al., 2020; Ling et al., 2019), which suggests various geologic processes in the regional evolution history. Based on the geologic maps and topographic and optical data, we identified outcrops of several prominent units including mare basalts, extraneous ejecta deposits, dome-like areas, and central peak of the Von Kármán crater (Fig. 1c). Mare basalts and the superposed ejecta deposits are clearly separated on the MI reflectance image of 1000 nm band where mafic minerals have conspicuous absorption (Fig. 1c). To investigate the geochemical characteristics of different units in the Von Kármán crater, the concentrations of FeO, TiO_2 and Th are extracted from the exact pixels of the outcrop locations shown in Fig. 1c. The results, along with the data of the CE-4 landing site, are shown in Fig. 4 and compared with the available bulk chemistry of the Apollo/Luna samples and lunar meteorites.

As shown in Fig. 4a, Th concentration in the four geologic units of the Von Kármán crater shows a narrow range (2.9–3.7 ppm). The relatively low concentration of Th suggests that this region is deficit of KREEP materials, which are widely distributed within the Procellarum KREEP Terrane (PKT) (Jolliff et al., 2000). In contrast, the FeO concentration shows relatively large variation, ranging from 6.8 to 18.4 wt.% (Fig. 4). Specifically, the central peak has the lowest FeO concentration (6.8–11.3 wt.%), suggesting a feldspathic-rich material (Korotev, 2005), while mare basalts contain FeO concentration of ~15 wt.% on average, which is consistent with typical lunar basaltic materials (Korotev, 2005). TiO_2 concentration of the Von Kármán mare and dome units varies from ~0.8 to 2.3 wt.%, and the mare materials excavated by fresh DHCs are ~0.9–1.8 wt.%, consistent with the very low-Ti (<1 wt.%) to low-Ti (1–6 wt.%) basalts (Neal and Taylor, 1992). While the feldspathic-rich central peak contains the lowest TiO_2 concentration that is generally less than 1 wt.%. Likely contaminated by basaltic material, the ejecta unit including the landing site is richer in TiO_2 than the central peak (Fig. 4b). The dome-like areas are compositionally (i.e., FeO, Th, and TiO_2) similar to the outcrops of mare basalts (Fig. 3a, b), indicating that they would have some petrologically genetic connections.

At the CE-4 landing site, the FeO concentration derived from Kaguya MI data is ~13.1 wt.% (Fig. 4), which is lower than the typical values of mare basalt samples (i.e., FeO >15 wt.%) and is higher than that of highland rocks (i.e., FeO <7 wt.%) (Korotev, 2005). Comparing with different geologic units, the landing site has a TiO_2 concentration (~1.8 wt.%) higher than most of the ejecta material and a medium FeO concentration between mare basalts and ejecta (Fig. 4b). Such intermediate FeO concentration suggests that the regolith at the CE-4 landing site are most likely a mixture of iron-rich mare components and iron-poor highland lithologies at or around the Von Kármán crater. LP GRS data show that the Th concentration at the CE-4 landing site is 3.55 ppm, which is distinctly lower than that of KREEP-bearing lithologies from Procellarum (>5 ppm) (Korotev, 1997). Compared with the Apollo and Luna regolith samples, the bulk chemical composition of the regolith at the CE-4 landing site (i.e., FeO and Th) is similar to the Apollo 15 soils (Fig. 4a).

Based on stratigraphic relationship and geologic context (in Section 1), a timeline for the formation of the geochemical units can be recognized. The central peak, low in iron and titanium concentrations, is the oldest unit that was formed simultaneously with the Von Kármán crater.

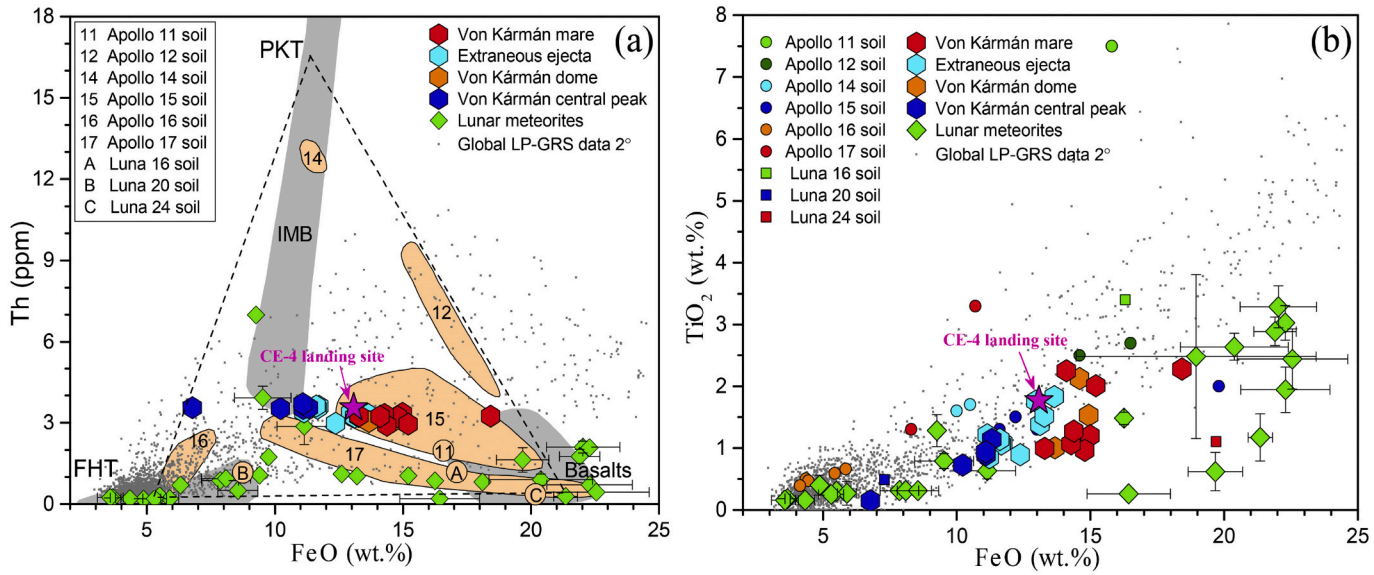

Fig. 4. (a) Th-FeO and (b) TiO_2-FeO concentrations of the locations marked in Fig. 1c. The bulk chemistry of the Apollo/Luna samples and lunar meteorites are also plotted for comparison (Korotev, 2005). The geochemical data of the CE-4 landing site is marked by the pink star. Gray dots are the global data from LP GRS observations with a spatial resolution of 2 degrees (Prettyman et al., 2006). PKT: Procellarum KREEP Terrane; FHT: Feldspathic Highlands Terrane; IMB: impact-melt breccia. (For interpretation of the references to colour in this figure legend, the reader is referred to the web version of this article.)

The most significant modification to the Von Kármán crater floor was the eruption of the iron-rich mare basalts at ~3.2 Ga (Lu et al., 2021). Endogenic processes also created two domes which have similar geochemistry with erupted mare basalts but might be formed in a later period (Head and Wilson, 2017). After the eruptions of mare basalts, emplacements of feldspathic ejecta from external craters (e.g., Finsen) covered a significant portion of the mare. In the landing region, geologic evidences indicate that the top layer is dominated by Finsen crater ejecta of low FeO concentration. Due to the processes in the following evolution, basaltic material might be mixed into the feldspathic ejecta and enhanced the local iron abundance.

3. Ejecta thickness estimation based on DHCs and non-DHCs

Our above geochemical analyses suggest that the floor of the Von Kármán crater is laterally inhomogeneous in composition and consists of two major components: the iron-rich mare basalts and the iron-poor non-mare ejecta. Subsurface structure, which can present the vertical extent of stratigraphic units, is another important aspect to understand the geologic evolution. The iron-poor CE-4 landing area is covered by feldspathic ejecta that were delivered from craters outside the Von Kármán crater. Thus, the thickness of the non-mare ejecta layer plays an important role in deriving the subsurface structure. In this work, we propose an approach to quantify the regional thickness distribution of non-mare ejecta in the CE-4 landing area using the excavation depth of DHCs and non-DHCs, which can complement the subsurface structure investigation with additional evidence. The method also provides a possible solution for calculating the thickness of ejecta overlaying on cryptomaria (Whitten and Head, 2015a; Whitten and Head, 2015b).

3.1. Identification of DHCs and non-DHCs

On the Moon, dark-haloed craters in optical images represent a special type of craters that are surrounded by a dark halo consisting of low-albedo ejecta (Antonenko et al., 1995; Bell and Hawke, 1984). Dark halo is especially prominent in the continuous ejecta facies that are about one radius from crater rim (Supplementary Fig. 1a), where crater ejecta are the most abundant. The low-albedo material is made of mare basalts that were buried by high-albedo non-mare ejecta and excavated during the cratering process of a DHC (Bell and Hawke, 1984; Schultz and Spudis, 1979). If the crater is not large enough to penetrate through the superposed ejecta deposits, the dark halo can not be formed and it appears as a non-DHC (Supplementary Fig. 1b). Based on the scaling relationship of crater diameter and its maximum excavation depth (Melosh, 1989), DHCs and non-DHCs can constrain the burial depth of mare basalts, i.e., the thickness of overlaying non-mare ejecta materials.

As the dark materials associated with DHCs are mare basalts that have a strong absorption at 1 μm band and thus is low in reflectance, optical images are effective data to distinguish DHCs and non-DHCs after eliminating the influence of maturity (Guo et al., 2019). In this study, we use Kaguya MI images (~20 m/pixel) of 1 μm band to identify DHCs and non-DHCs. As shown in Fig. 2, the OMAT does not display significant variations among different areas. In the CE-4 landing area, low albedo materials of DHCs can extend to 1–3 radii from crater rims. Examples of a typical DHC and a non-DHC in the investigation area can be seen in Supplementary Fig. 1. As observed at a low altitude by the CE-4 landing camera (Supplementary Fig. 2), DHCs are widely distributed on the Von Kármán crater floor. In the ~40 km × 40 km region around the CE-4 landing site (i.e., Statio Tianhe), 35 DHCs (with diameters of ~277–1422 m) and 50 non-DHCs (with diameters of ~181–531 m) were identified and mapped out (Fig. 5, Supplementary Table 3). Both DHCs and non-DHCs have similar optical maturity (OMAT) distribution (Supplementary Fig. 3), and therefore the dark halos are not caused by regolith maturity. Spatial distribution in Fig. 5 shows that more DHCs were identified in the southwest than in the northeast, indicating that ejecta in the northeast region are probably relatively thicker. At the CE-4 landing site, the closest DHC to the CE-4 landing site is much further than the closest non-DHC, which may suggest that the landing site locates in a region with relatively thick ejecta deposits.

3.2. Method for ejecta thickness estimation

A direct way to obtain the thickness of extraneous ejecta overlaying the mare basalt is to identify the ejecta-mare interface, and the ejecta thickness can be easily obtained by subtracting the elevation of the interface from the surface elevation. As the ejecta-mare interface is spatially continuous and lays between the deepest excavations of DHCs and non-DHCs, these two types of craters can be used to constrain

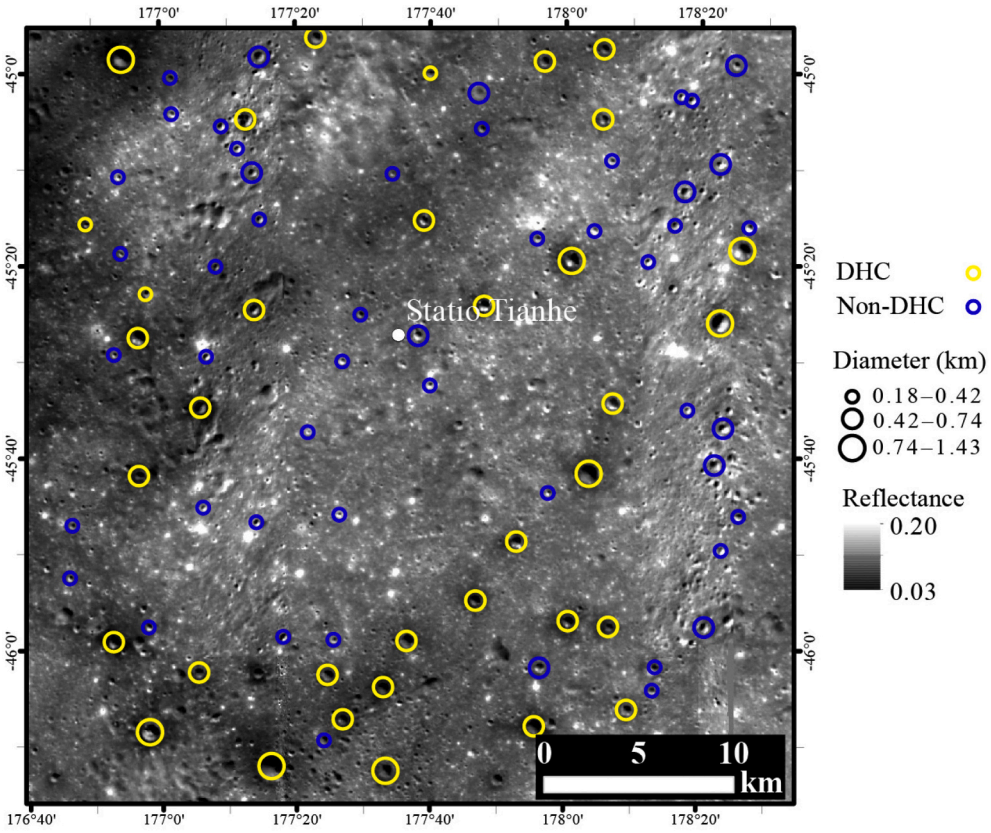

Fig. 5. The DHCs (yellow) and non-DHCs (blue) identified in the area around the CE-4 landing site. The circle size represents the relative size of three diameter groups instead of the real diameters. Background image is the MI reflectance at 1000 nm band. Statio Tianhe (white dot) is the landing site of the CE-4 mission. (For interpretation of the references to colour in this figure legend, the reader is referred to the web version of this article.)

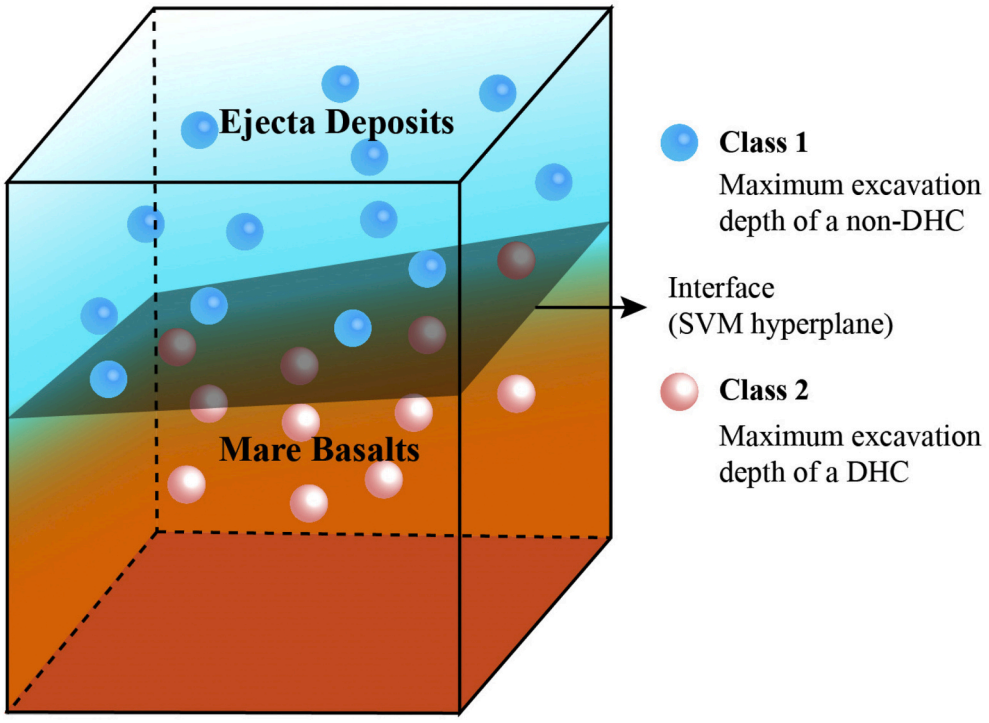

Fig. 6. A schematic diagram showing the SVM algorithm used to estimate the thickness of ejecta deposits. Each ball represents the maximum excavation depth of a non-DHC (blue) or DHC (red). (For interpretation of the references to colour in this figure legend, the reader is referred to the web version of this article.)

locations of the ejecta-mare interface. From another perspective, the ejecta-mare interface can be regarded as a classifier that can ideally separate the DHCs and non-DHCs by their maximum excavate depths, as demonstrated in Fig. 6. In this study, a classifier is generated from DHCs and non-DHCs data using the support-vector machine (SVM) model (Cortes and Vapnik, 1995). The hyperplane of the derived classifier represents the ejecta-mare interface (Fig. 6). As a widely-used supervised machine learning model, SVM can make good use of the training data by calculating the data in other dimensions in which different classes can be separated more accurate. The hyperplane of SVM classifier is defined as the plane that has the largest distance to different classes in multi-dimensional space (Cortes and Vapnik, 1995). In SVM, the kernel function is flexible to be defined to meet the requirements of the specified application scenarios. The theoretical basis of SVM algorithm can be found in Appendix A.

Our estimate of the ejecta thickness is implemented through several steps. First, calculating the maximum excavation depths (h_e) of DHCs and non-DHCs. For simple craters (usually <20 km in diameter), cratering mechanism analysis suggests that the maximum excavation depth is about 1/10 of the transient cavity diameter, which is about 0.84 of the rim-to-rim diameter (Melosh, 1989). Thereafter, the background elevation (h) of each crater is extracted from SELENE and LRO DEM 2015 (SLDEM2015) lunar DEM model (~60 m/pixel), which has the vertical accuracy of ~3–4 m (Barker et al., 2016). To exclude the ejecta from the crater itself, h is defined as the mean elevation of the annulus 2.5–3 radii from the crater center. With the results of the above two steps, we can get the elevation at the maximum cratering excavation (z) through h-h_e. The three-dimensional coordinates of crater maximum excavation make up the training vectors ($[x_i, y_i, z_i]$, where x_i and y_i are the horizontal coordinates of a crater center, i represents the crater index). Two target values for classification ($[k_i]$) are self-defined (such as 1 and − 1) to represent DHC and non-DHC, respectively. Through SVM training, we can obtain the classification hyperplane, which shows the location of the ejecta-mare interface. By subtracting hyperplane from the regional elevation, thickness of the extraneous ejecta can be obtained.

In this study, the SVM process is implemented using scikit-learn package (https://scikit-learn.org/), a machine learning module for Python. Penalty parameter C and kernel parameter γ are the most important parameters in our SVM model with radial basis function (RBF) kernel. As the parameter γ increases, the hyperplane becomes more complex and has higher accuracy, but may result in overfitting at large γ. Meanwhile, a larger C value also gives higher accuracy with the risk of overfitting. On the contrary, smaller γ and C result in lower accuracy and may be underfitted.

We tested parameter C from 5 to 100 and parameter γ from 0.1 to 10 (Appendix A). Part of the results is shown in Supplementary Fig. 4. To avoid either underfitting or overfitting, we finally chose the results of $C = 30$ and $\gamma =$ 'scale' (≈4) (Supplementary Fig. 4; Supplementary Tables 1 and 3; Supplementary Movie 1). With 2 DHCs and 4 non-DHCs outliers in the 85 training craters, the accuracy score of our SVM classifier is 0.93 (79/85, Supplementary Tables 1 and 3), which means that 93% of the DHCs and non-DHCs can be correctly separated by the classifier hyperplane. It indicates that the mare-ejecta interface is well-modeled by the SVM hyperplane.

3.3. Ejecta thickness estimation results

Using the SVM model, we obtained the three-dimensional coordinates of ejecta-mare interface, i.e., the hyperplane of the SVM classifier (Fig. 6). By subtracting the elevation of the interface from SLDEM2015, thickness distribution of the non-mare ejecta in the CE-4 landing area is calculated and is shown in Fig. 7. Instead of only getting the range of areal ejecta thickness (e.g., Li et al., 2020), we obtained the thickness value at every location of the investigation area, which provides important information for understanding geology and materials of the CE-4 landing area. Spatial resolution of the thickness data is 60 m/pixel, which is the same as the DEM model SLDEM2015 (Barker et al., 2016). As shown in Fig. 7a, the ejecta show a southwest-northeast distribution pattern and are thicker in the northeast, indicating that Finsen crater is one of the important ejecta sources. The distance (117–166 km) of the investigation area is more than one radius away

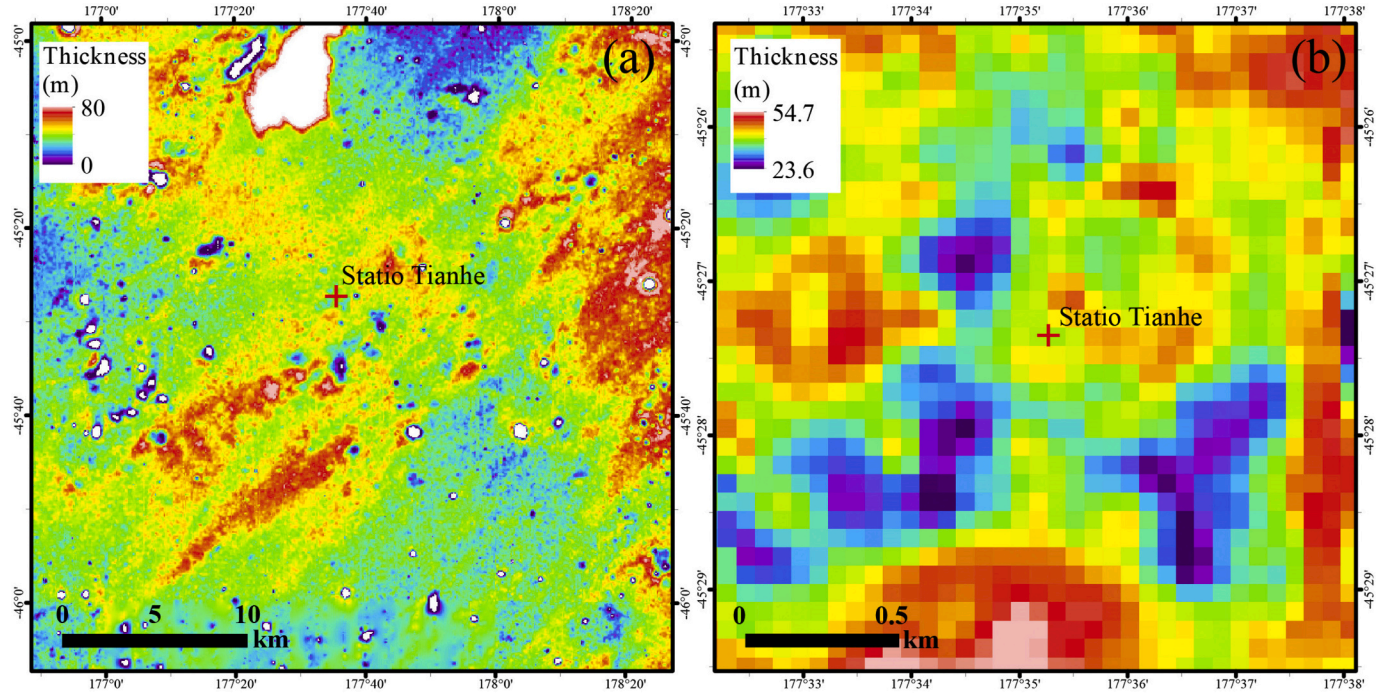

Fig. 7. (a) Ejecta thickness map for the region 40 km across the CE-4 landing site (Statio Tianhe). (b) Ejecta thickness in local area of the CE-4 landing site. The spatial resolution is 60 m/pixel. To get rid of the invalid ejecta thickness estimate in the region, the pixels are obliterated and shown in white if the thickness value is negative (e.g., floor of large craters) or greater than 80 m (e.g., the central peak), which is almost the deepest excavation of the identified craters.

from the rim of the Finsen crater, therefore the ejecta are discontinuous and appear as linear ridges up to tens of meters high (Fig. 1d, Fig. 7a, Supplementary Fig. 5). The thickest ejecta in the investigation region is ~80 m whereas some areas are nearly free of non-mare ejecta (Fig. 7a), and the mean thickness is 41 m. At the CE-4 landing site, the ejecta are ~40 m thick (Fig. 7b), and the uncertainty is less than 2 m according to LPR detections (Section 4). Due to the nonuniform distribution of the ejecta, there is a substantial variation of ~30 m even within a region of 100 s m across (Fig. 7b).

There are several factors that may affect the accuracy of the SVM classifier and result in errors in the ejecta thickness estimate. (1) Impact experiments suggest that a dark-haloed crater can not be created until the excavation penetrates in the mare basalts deeper than just touching the pre-existing mare surface (Antonenko, 1999). Thus, the calculated ejecta thickness is likely overestimated to some extent. However, no reliable correction methods can be applied at present. (2) The rough terrain surface around the crater causes uncertainty in the background elevation estimation, which can be seen from the standard deviation (2.1–23.5 m) of crater background elevation in Supplementary Table 3. This effect can be minimized as SVM classifier is produced from the entire crater database. After excluding the three craters with unusually large DEM standard deviations (> 10 m) (Supplementary Table 3), we got almost the same ejecta thickness of ~40 m at the landing site. (3) The nonuniform distribution of craters, especially the absence of either DHCs or non-DHCs in sub-areas can lead to poor constraints and increase the uncertainties at local scale, such as the area southwest to the CE-4 landing site where no DHCs are observed. Nevertheless, such problems can not be removed even using other methods, and the results of this study can be compared with in situ observations of the CE-4 LPR.

4. Ejecta thickness based on the CE-4 LPR observations

CE-4 LPR is a dual-frequency ground penetrating radar operating at center frequencies of 60 and 500 MHz (Fang et al., 2014). According to the Kaguya MI observations, the FeO and TiO_2 concentrations of the regolith at the CE-4 landing site are 12.7 wt.% and 1.3 wt.%, respectively. Using the relation among dielectric permittivity, bulk density, and composition of regolith (Fa and Wieczorek, 2012) and a typical porosity of 0.45, dielectric permittivity of the lunar surface materials at the landing site is estimated to be $3.07 + 0.020i$. Such extremely low loss tangent (0.0064) of the surface material allows the radar waves penetrate as deep as several tens of meters, providing a chance to constrain the ejecta thickness. Here we compare the estimated ejecta thickness with the in situ LPR high-frequency observations during the first lunar

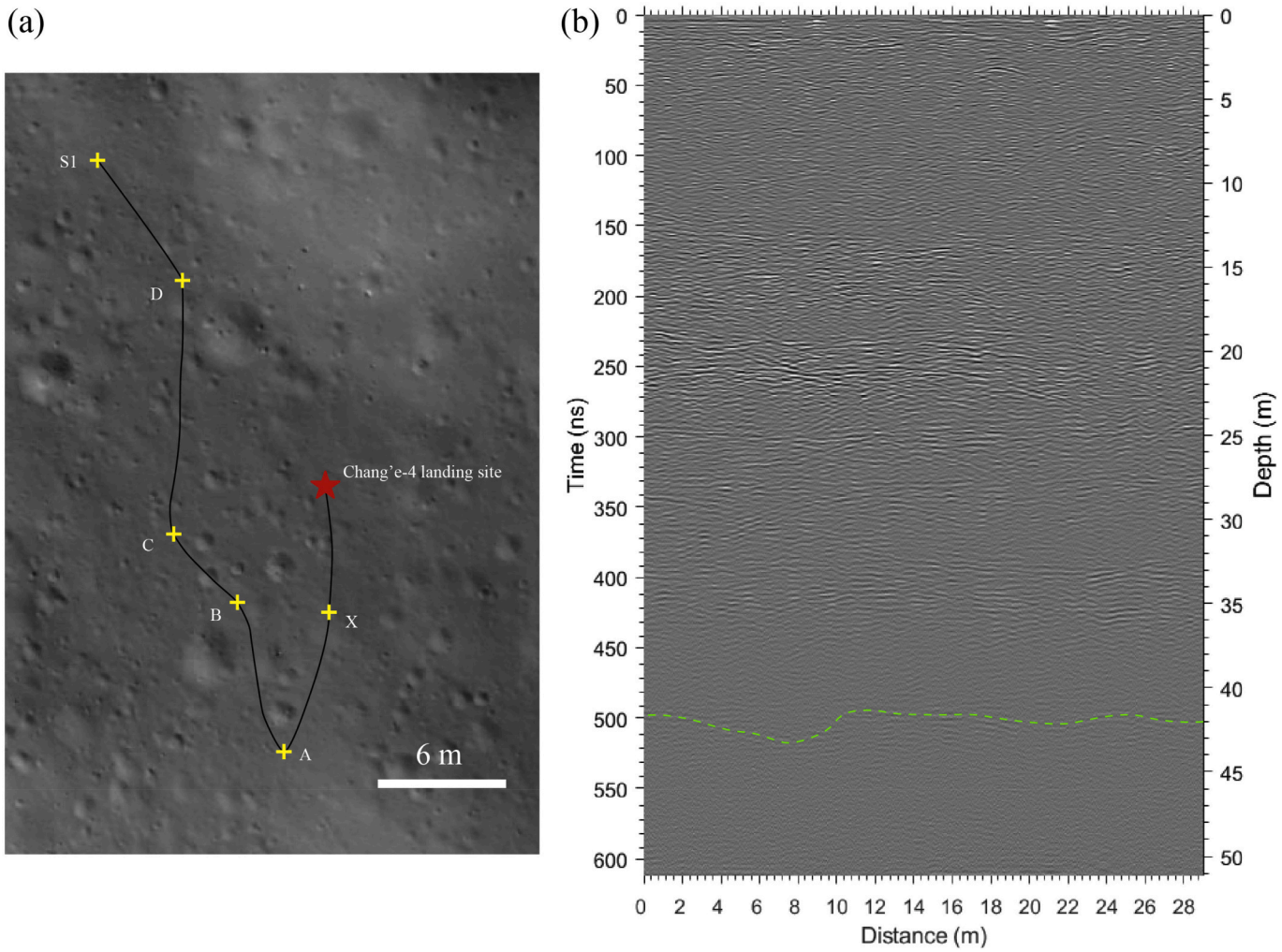

Fig. 8. (a) An optical image from the CE-4 landing camera (LCAM, image ID: CE4_GRAS_LCAM-1-3050_SCI_N_20190103022520_20190103022520_0001_A) showing the geologic context of the landing site; the red star is the CE-4 landing site; the black line shows the traverse line of the Yutu-2 rover; and X, A, B, C, D and S1 are surface navigation points during the first lunar day. (b) The processed LPR image from Point A to S1 along the Yutu-2 survey line. The green dashed line shows the deepest echoes at a depth of ~42 m. The one-way travel time between the antenna and the surface is offset so that zero time corresponds to the lunar surface, and the depth is obtained with a real dielectric permittivity of 3.1. (For interpretation of the references to colour in this figure legend, the reader is referred to the web version of this article.)

day.

During the first lunar day (Fig. 8a), the rover traveled from point X to S1, with a surface traverse of ~37.8 m, which is in a pixel size of the non-mare ejecta thickness data (Fig. 7). After removing the repetitive observations at the navigation points (e.g., points X, A, B, C, D, and S1), there are in total 1038 effective tracks of raw data for the high frequency channel. From point X to A, it is the parameters adjustment period. Cumulative number of the LPR was adjusted until to point A, and a constant value of 12 was set. Therefore, we selected 880 tracks of LPR data from point A to S1, and the surface traverse is ~29 m. The raw data were then processed following the standard ground penetrating radar (GPR) data processing procedure, including horizontal band removal, band-pass filtering, and compensation of geometrical spreading and dielectric attenuation (e.g., Fa et al., 2020; Fa et al., 2015). The processed LPR image is shown in B-scan format as a function of lateral distance (horizontal) and one-way travel time (vertical), or equivalently, depth (Fig. 8b). To convert the time delay to depth, a real dielectric permittivity of 3.1 is used. Absolute signal amplitude calibration is not conducted at the moment and the tone in Fig. 8b shows the relative amplitude with white representing strong echoes and gray denoting weak echoes.

In Fig. 8b, a homogenous region is obvious from the surface to a depth of ~11–14 m. This region contains many random irregular layers with lateral continuity only a few meters, and several hyperbolic curves, which are most probably caused by subsurface rocks of sizes larger than ~0.35 m (the wavelength of the LPR waves) (Fa et al., 2015). Below this layer to a depth of ~36–38 m is a region that appears bright and dark alternatively from the top to the bottom. Within this region, two echoes at a depth of ~25 m and ~27.5 m are very obvious. The deepest echo can be detected is at ~42 m, though very weak. Below 42 m is a region with random noises that is beyond the penetration ability of the high-frequency LPR. Here the weak echo at a depth of ~42 m could be the base of the ejecta, and this value is also consistent with the estimate from DHCs and non-DHCs (Section 3). The ejecta thickness constrained from DHCs is 40 m, and the LPR observations show that subsurface to a depth of 42 m is inhomogeneous at the CE-4 landing site. This implies that the ejecta at the CE-4 landing site are mostly probably accumulated from multiple impact events, as evidenced by the secondary crater chains in different directions (Section 1).

5. Discussion

Based on our analyses, the ejecta thickness of the CE-4 landing region is highly nonuniform and ranges from near zero to ~80 m, and the thickness at the landing site is ~40 m. Comparing with previous studies (e.g., Di et al., 2019; Huang et al., 2018; Lai et al., 2019; Li et al., 2020), our study used both geologic analysis (DHCs and non-DHCs) and in situ LPR observations, and the results are consistent with each other. In the local region around the CE-4 landing site, we identified six DHCs and non-DHCs (denoted by C1 to C6, Fig. 9), which can provide close constraints to the ejecta thickness at local scale. As can be seen in Fig. 9, the nearest DHC is crater C2, ~565 m in diameter situated in the northeast and is ~4.7 km from the landing site, and the nearest non-DHC is crater C5, ~452 m in diameter situated at ~1 km from the landing site in the east. Based on scaling relation estimation (Melosh, 1989), the maximum excavation depths of the DHC (C2) and the non-DHC (C5) are about 47 m and 38 m, respectively. The elevation of the CE-4 landing site is almost the same as the background elevation of crater C5, but is ~7 m lower than that of crater C2. Based on these craters, the ejecta thickness at the CE-4 landing site is ~40 m, which is in agreement with the values based on SVM estimate and LPR observations.

There are several craters located around the Von Kármán crater (Fig. 1a), three of them might deliver non-mare ejecta to the CE-4 landing site, including Finsen, Von Kármán L, Von Kármán L' (Supplementary Table 2). The Alder crater was also considered as an ejecta source (e.g., Di et al., 2019), but a latest study suggests that its age is

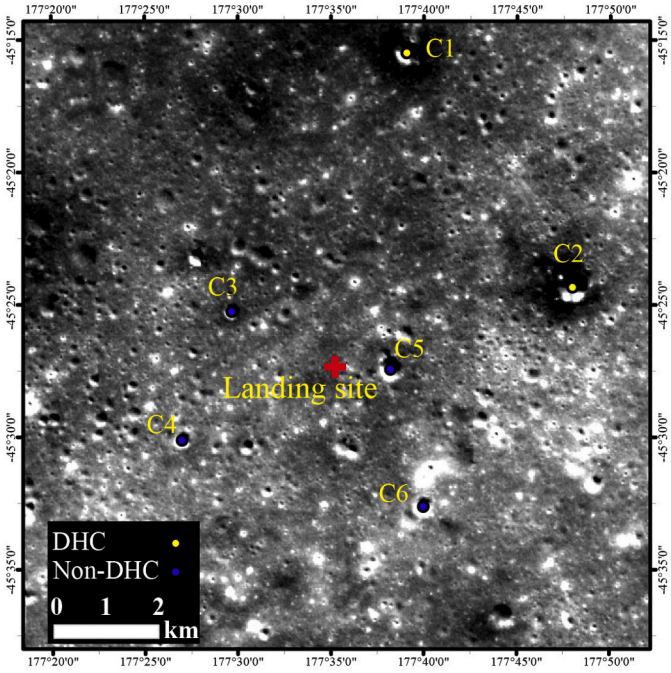

Fig. 9. DHCs (yellow) and non-DHCs (blue) near the CE-4 landing site. The diameters of craters C1, C2, C3, C4, C5 and C6 are 480, 565, 319, 316, 452 and 363 m, respectively. Background is MI reflectance image of 1000 nm band. (For interpretation of the references to colour in this figure legend, the reader is referred to the web version of this article.)

older than the mare units (Lu et al., 2021). As Zhinyu crater is small (3.8 km in diamter) and is far (>15 km) from the study area, its influence to the ejecta thickness of the CE-4 landing area is negligible. In order to evaluate the major ejecta sources, we modeled the accumulated ejecta thickness based on crater ejecta thickness decay model of Pike (1974); and the mixture process with local material was considered in modeling (Oberbeck et al., 1975). Model equations are given in Supplementary Text 1. The results suggest that the accumulated ejecta are ~9.5 m thick at the CE-4 landing site (Supplementary Fig. 7). The value is significantly less than SVM estimates and LPR observations. One reason is that the landing site is located outside of the continuous ejecta of all the three craters, where the ejecta are sedimented alternately and the thickness variation can not be predicted by ejecta thickness decay laws. The original data from which the model was generated also show great variety in discontinuous ejecta facies (McGetchin et al., 1973; Pike, 1974). Moreover, we only considered three craters in the modeling, but young craters from further distances could also contribute ejecta materials. Based on cratering simulation of Di et al. (2019), ejecta from Finsen crater could be ~30 m thick at the CE-4 landing site, which is also inconsistent with ejecta decay model but is close to our estimates. Though absolute ejecta thickness was not well predicted by the ejecta decay model, the relative thickness can be concluded. At the landing site, calculation from the Pike's model suggests that ejecta from Finsen crater are ~4 m, from Von Kármán L and Von Kármán L' are both less than 1 m, and that about half of the accumulated ejecta are excavated local material. Therefore, the superposed non-mare materials are mainly a mixture of Finsen crater ejecta and excavated mare basalts, and the fraction of local material increases with depth (Xie et al., 2020). The ejecta-mare mixture scenario is also consistent with the geochemical characteristics (Section 2).

Located in the region of ~4.2 Ga old Von Kármán crater, the CE-4 landing area has a complex evolution history. Geochemical analysis indicates that the surface of the Von Kármán crater floor consists of two major compositional components: the iron-rich mare basalts and the iron-poor non-mare ejecta. The youngest of the major ejecta suppliers is

Finsen crater. At the CE-4 landing site, the non-mare ejecta are ~40 m thick and the materials are mainly a mixture of Finsen crater ejecta and excavated mare basalts during sedimentation, in which the fractions of mare materials increase with depth. Geochemistry of the landing site also shows an intermediate FeO concentration between mare basalts and feldspathic highland material. After the sedimentations of extraneous ejecta, due to space weathering processes such as micrometeorite bombardments and solar wind implantation, the primary ejecta have been shattered and overturned to some depth. On the other hand, postdated impact events could excavate and transport basaltic materials to the surface, as shown in Supplementary Fig. 6. Therefore, it is expected that the materials observed by VNIS on the Yutu-2 rover are predominated by the feldspathic ejecta from the Finsen crater with a significant portion of basaltic materials (e.g., Hu et al., 2019; Lin et al., 2019).

Our study quantified the compositional variations in different geologic units of the Von Kármán crater floor. The CE-4 spacecraft landed in an area dominated by ejecta from Finsen crater and its geochemical characteristics are distinct from typical mare basalts, which is consistent with previous studies (e.g., Huang et al., 2018; Lin et al., 2019; Ling et al., 2019). The SVM algorithm employed in our study revealed regional thickness of extraneous ejecta of the CE-4 landing area, shedding new light on the regional geologic evolution. Supported by LPR observations and local geologic features, we estimated that the ejecta thickness at the CE-4 landing site is ~40 m, which is consistent with Li et al. (2020) but inconsistent with other studies (e.g., Di et al., 2019; Huang et al., 2018; Lai et al., 2019).

6. Conclusions

In this work, we explored the geochemical characteristics and non-mare ejecta distribution of the Von Kármán crater with special emphasis on the landing area of the Chang'e-4 probe. Geochemistry of the Von Kármán crater indicates that the regolith in the CE-4 landing area is distinct from typical mare basalts. Geologic characteristics and the concentrations of FeO, TiO_2 and Th indicate that the landing site materials are mixed from feldspathic ejecta and mare basalts, with Finsen crater ejecta material as a major component. To address the thickness of superposed ejecta above mare basalts, we identified and analyzed 35 DHCs and 50 non-DHCs in the landing area. By adopting the SVM algorithm, we obtained the equivalent ejecta-mare interface and calculated the thickness of non-mare ejecta over the CE-4 landing region. The results suggest that the ejecta thickness is substantially varied and is ~40 m at the landing site, in agreement with the LPR measurements of the reflectors boundary at ~42 m depth. Based on ejecta distribution models, Finsen crater is the major source of foreign ejecta accumulated at the CE-4 landing site and a significant portion of local materials are mixed to the non-mare ejecta. Results from this work demonstrated important properties of the materials in the Chang'e-4 landing area in a broad view and at specified locations, which can be used in the Yutu-2 data interpretation and rover traverse design, e.g., searching for mare basalts outcrops where non-mare ejecta are thin.

Declaration of Competing Interest

The authors declare no competing interests.

Acknowledgments

This work was supported partly by B-type Strategic Priority Program of the Chinese Academy of Sciences (No. XDB41000000), National Natural Science Foundation of China (No. 41902317, 41941002, 41773065), National Key Research and Development project (2019YFE0123300) and China Postdoctoral Science Foundation (No. 2019M650319). SLDEM2015 and Th concentration data can be found in the NASA's Planetary Data System (http://pds.nasa.gov/). The Kaguya MI data are archived at SELENE Data Archive (https://darts.isas.jaxa.jp/planet/pdap/selene/). The CE-4 data are provided by China National Space Administration, and are available at Data Publishing and Information Service System of China's Lunar Exploration Program (http://moon.bao.ac.cn/). The authors acknowledge editor Brandon Johnson for handling the manuscript. We thank Noah Petro, James W. Head and an anonymous reviewer for helpful comments that improved the manuscript. This is PKU PRSL contribution 15.

Supplementary data to this article can be found online at https://doi.org/10.1016/j.icarus.2021.114327.

Appendix A. Support-vector machine (SVM)

A support-vector machine is a learning machine originally for two-group classification problems (Cortes and Vapnik, 1995). Given the training data:

$$(\vec{x_1}, y_1), \ldots, (\vec{x_n}, y_n) \tag{A1}$$

where $\vec{x_i}$ is a p-dimensional vector, y_i is either -1 or 1, representing which class the point $\vec{x_i}$ belongs to. The SVM classifier is defined by finding the optimal (p-1)-dimensional hyperplane, which has the maximum distance from the nearest point of either $y_i = -1$ class or $y_i = 1$ class. The hyperplane can be expressed as

$$\vec{w} \cdot \vec{x} + b = 0 \tag{A2}$$

where $\vec{w}$ is the normal vector to the hyperplane, and b is the bias (Fig. A1). If the training data are linearly separable, the margins of the two groups can be defined as:

$$\vec{w} \cdot \vec{x} + b = -1 \tag{A3}$$

$$\vec{w} \cdot \vec{x} + b = 1 \tag{A4}$$

The points located on the margins are called support vectors. For any data $\vec{x_i}$ in the class of $y_i = 1$,

$$\vec{w} \cdot \vec{x_i} + b \geq 1 \tag{A5}$$

For $\vec{x_i}$ in the class of $y_i = -1$,

$$\vec{w} \cdot \vec{x_i} + b \leq -1 \tag{A6}$$

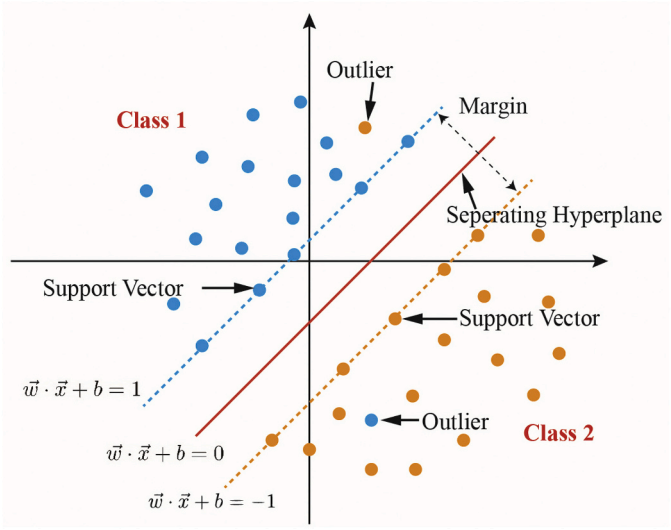

Fig. A1. Schematic diagram of SVM classifier. The two classes are represented by points in orange ($y=-1$) and blue ($y=1$), respectively. (For interpretation of the references to colour in this figure legend, the reader is referred to the web version of this article.)

SVM works when the training data are linearly separable, which, however, is hard to be satisfied in most actual scenarios. Therefore, kernel functions are usually employed to map $\vec{x_i}$ to $\varnothing(\vec{x_i})$, which is more separable than original data (Cortes and Vapnik, 1995). The kernel function can be self-defined or taken from the generally used ones such as linear function, polynomial function, or radial basis function (RBF). RBF has the ability to project the original data space into infinite dimensional space by adjusting the parameters and is very flexible (Shawe-Taylor and Cristianini, 2004). In RBF kernel, the value of a given point depends on the distance of the other points, the closer ones have stronger influence, which meets the Tobler's first law of geography (Tobler, 1970), and thus used in our process.

SVM training with RBF kernel uses two parameters to control the fitting results, C and γ. Their effects to the classifier can be seen in Supplementary Fig. 4. The parameter C is the penalty parameter and is common to all SVM kernels. A low C makes the decision surface smooth and has the risk of underfitting, while a high C aims at classifying all training examples correctly and has the risk of overfitting (Ben-Hur and Weston, 2010). The decision of parameter C is a trade-off between the margin and the size of the slack variables in specified cases (Shawe-Taylor and Cristianini, 2004). The parameter γ, $\gamma = 1/(2\sigma^2)$ (where σ is the standard deviation), decides how far the influence of a single training example reaches, and the influence distance is further with smaller value and vice versa (Ben-Hur and Weston, 2010). If γ is too large, the influence of support vectors only reaches the support vector itself; while if γ is too small, the support vectors would influence the whole training set and the model cannot capture the complexity or "shape" of the data.

References

Antonenko, I., 1999. Volumes of Cryptomafic Deposits on the Western Limb of the Moon: Implications for Lunar Volcanism. Department of Geological Sciences, Brown University.

Antonenko, I., Head, J.W., Mustard, J.F., Hawke, B.R., 1995. Criteria for the detection of lunar cryptomaria. Earth Moon Planet. 69 (2), 141–172. https://doi.org/10.1007/Bf00613096.

Barker, M.K., Mazarico, E., Neumann, G.A., Zuber, M.T., Haruyama, J., Smith, D.E., 2016. A new lunar digital elevation model from the lunar orbiter laser altimeter and SELENE terrain camera. Icarus. 273, 346–355. https://doi.org/10.1016/j.icarus.2015.07.039.

Bell, J.F., Hawke, B.R., 1984. Lunar dark-haloed impact craters: origin and implications for early mare volcanism. J. Geophys. Res. 89 (B8), 6899–6910. https://doi.org/10.1029/JB089iB08p06899.

Ben-Hur, A., Weston, J., 2010. A user's guide to support vector machines. In: Carugo, O., Eisenhaber, F. (Eds.), Data Mining Techniques for the Life Sciences. Humana Press, Totowa, New Jersey, pp. 223–239. https://doi.org/10.1007/978-1-60327-241-4_13.

Charlier, B., Grove, T.L., Namur, O., Holtz, F., 2018. Crystallization of the lunar magma ocean and the primordial mantle-crust differentiation of the moon. Geochim. Cosmochim. Acta 234, 50–69. https://doi.org/10.1016/j.gca.2018.05.006.

Cortes, C., Vapnik, V., 1995. Support-vector networks. Mach. Learn. 20 (3), 273–297. https://doi.org/10.1007/BF00994018.

Di, K., Zhu, M.H., Yue, Z., Lin, Y., Wan, W., Liu, Z., Gou, S., Liu, B., Peng, M., Wang, Y., Niu, S., Zhang, J., Li, J., Xie, J., Xi, L., Yang, J., Xue, B., 2019. Topographic evolution of Von Kármán crater revealed by the lunar rover Yutu-2. Geophys. Res. Lett. 46 (22), 12764–12770. https://doi.org/10.1029/2019gl085252.

Elkins-Tanton, L.T., Burgess, S., Yin, Q.Z., 2011. The lunar magma ocean: reconciling the solidification process with lunar petrology and geochronology. Earth Planet. Sci. Lett. 304 (3–4), 326–336. https://doi.org/10.1016/j.epsl.2011.02.004.

Fa, W., Wieczorek, M.A., 2012. Regolith thickness over the lunar nearside: results from earth-based 70-cm Arecibo radar observations. Icarus. 218 (2), 771–787. https://doi.org/10.1016/j.icarus.2012.01.010.

Fa, W., Zhu, M.-H., Liu, T., Plescia, J.B., 2015. Regolith stratigraphy at the Chang'E-3 landing site as seen by lunar penetrating radar. Geophys. Res. Lett. 42 (23), 10179–10187. https://doi.org/10.1002/2015gl066537.

Fa, W., Guo, D., Liu, X., Du, J., 2020. Shallow subsurface structure of the moon at China's Chang'E 4 landing site observed by the lunar penetrating radar. In: The 51st Lunar and Planetary Sciecne Conference (p. #1799).

Fang, G.-Y., Zhou, B., Ji, Y.-C., Zhang, Q.-Y., Shen, S.-X., Li, Y.-X., Guan, H.-F., Tang, C.-J., Gao, Y.-Z., Lu, W., Ye, S.-B., Han, H.-D., Zheng, J., Wang, S.-Z., 2014. Lunar penetrating radar onboard the Chang'e-3 mission. Res. Astron. Astrophys. 14 (12), 1607–1622. https://doi.org/10.1088/1674-4527/14/12/009.

Fortezzo, C.M., Spudis, P.D., Harrel, S.L., 2020. Release of the digital unified global geologic map of the Moon at 1:5,000,000-scale. In: Lunar and Planetary Science Conference (p. #2760).

Garrick-Bethell, I., Zuber, M.T., 2005. An indigenous origin for the south pole Aitken basin thorium anomaly. Geophys. Res. Lett. 32, L13203 https://doi.org/10.1029/2005gl023142.

Garrick-Bethell, I., Zuber, M.T., 2009. Elliptical structure of the lunar south pole-Aitken basin. Icarus 204 (2), 399–408. https://doi.org/10.1016/j.icarus.2009.05.032.

Garrick-Bethell, I., Miljković, K., Hiesinger, H., van der Bogert, C.H., Laneuville, M., Shuster, D.L., Korycansky, D.G., 2020. Troctolite 76535: a sample of the moon's south pole-Aitken basin? Icarus 338, 113430. https://doi.org/10.1016/j.icarus.2019.113430.

Gou, S., Di, K., Yue, Z., Liu, Z., He, Z., Xu, R., Lin, H., Liu, B., Peng, M., Wan, W., Wang, Y., Liu, J., 2019. Lunar deep materials observed by Chang'e-4 rover. Earth Planet. Sci. Lett. 528, 115829. https://doi.org/10.1016/j.epsl.2019.115829.

Guo, D., Fa, W., Zeng, X., Cai, Y., Du, J., Zhao, M., 2019. Geological investigation of the Chang'e-4 landing site and the expected scientific return from the lunar penetrating radar. In: The 50th Lunar and Planetary Science Conference (#1844).

Haskin, L.A., McKinnon, W.B., Benner, L.A.M., Jolliff, B.L., 2004. Thorium anomalies in the NW quadrant of the South Pole-Aitken basin. In: The 35th Lunar and Planetary Science Conference (#1461).

Head, J.W., Wilson, L., 2017. Generation, ascent and eruption of magma on the moon: new insights into source depths, magma supply, intrusions and effusive/explosive eruptions (part 2: predicted emplacement processes and observations). Icarus 283, 176–223. https://doi.org/10.1016/j.icarus.2016.05.031.

Hu, X., Ma, P., Yang, Y., Zhu, M.-H., Jiang, T., Lucey, P.G., Sun, L., Zhang, H., Li, C., Xu, R., He, Z., Lin, H., Huang, C., Sun, Y., 2019. Mineral abundances inferred from in situ reflectance measurements of Chang'e-4 landing site in south pole-Aitken basin. Geophys. Res. Lett. 46 (16), 9439–9447. https://doi.org/10.1029/2019GL084531.

Huang, J., Xiao, Z., Flahaut, J., Martinot, M., Head, J., Xiao, X., Xie, M., Xiao, L., 2018. Geological characteristics of Von Kármán crater, northwestern south pole-Aitken basin: Chang'e-4 landing site region. J. Geophys. Res. Planet. 123 (7), 1684–1700. https://doi.org/10.1029/2018JE005577.

Jia, Y., Zou, Y., Ping, J., Xue, C., Yan, J., Ning, Y., 2018. The scientific objectives and payloads of Chang'E−4 mission. Planet. Space Sci. 162, 207–215. https://doi.org/10.1016/j.pss.2018.02.011.

Jolliff, B.L., Gillis, J.J., Haskin, L.A., Korotev, R.L., Wieczorek, M.A., 2000. Major lunar crustal terranes: surface expressions and crust-mantle origins. J. Geophys. Res. Planet. 105 (E2), 4197–4216. https://doi.org/10.1029/1999je001103.

Jolliff, B.L., Shearer, C.K., Papanastassiou, D.A., Liu, Y., 2017. Why do we need samples from the Moon's South Pole-Aitken basin and what would we do with them?. In: The 48th Lunar and Planetary Science Conference (#1300).

Korotev, R.L., 1997. Some things we can infer about the moon from the composition of the Apollo 16 regolith. Meteorit. Planet. Sci. 32 (4), 447–478. https://doi.org/10.1111/j.1945-5100.1997.tb01291.x.

Korotev, R.L., 2005. Lunar geochemistry as told by lunar meteorites. Geochemistry 65 (4), 297–346. https://doi.org/10.1016/j.chemer.2005.07.001.

Lai, J., Xu, Y., Zhang, X., Xiao, L., Yan, Q., Meng, X., Zhou, B., Dong, Z., Zhao, D., 2019. Comparison of dielectric properties and structure of lunar regolith at Chang'e-3 and Chang'e-4 landing sites revealed by ground-penetrating radar. Geophys. Res. Lett. 46 (22), 12783–12793. https://doi.org/10.1029/2019gl084458.

Lawrence, D.J., Feldman, W.C., Barraclough, B.L., Binder, A.B., Elphic, R.C., Maurice, S., Miller, M.C., Prettyman, T.H., 2000. Thorium abundances on the lunar surface. J. Geophys. Res.-Planet. 105 (E8), 20307–20331. https://doi.org/10.1029/1999je001177.

Lawrence, D.J., Elphic, R.C., Feldman, W.C., Gasnault, O., Genetay, I., Maurice, S., Prettyman, T.H., 2002. Small-area thorium enhancements on the lunar surface. In: The 33rd Lunar and Planetary Science Conference (#1970).

Lemelin, M., Lucey, P.G., Song, E., Taylor, G.J., 2015. Lunar central peak mineralogy and iron content using the Kaguya multiband imager: reassessment of the compositional structure of the lunar crust. J. Geophys. Res. Planet. 120 (5), 869–887. https://doi.org/10.1002/2014JE004778.

Lemelin, M., Lucey, P.G., Gaddis, L.R., Hare, T., Ohtake, M., 2016. Global map products from the Kaguya Multiband Imager at 512 ppd: Minerals, FeO, and OMAT. In: The 47th Lunar and Planetary Science Conference (#2994).

Li, C., Liu, D., Liu, B., Ren, X., Liu, J., He, Z., Zuo, W., Zeng, X., Xu, R., Tan, X., Zhang, X., Chen, W., Shu, R., Wen, W., Su, Y., Zhang, H., Ouyang, Z., 2019. Chang'E-4 initial spectroscopic identification of lunar far-side mantle-derived materials. Nature 569 (7756), 378–382. https://doi.org/10.1038/s41586-019-1189-0.

Li, C., Su, Y., Pettinelli, E., Xing, S., Ding, C., Liu, J., Ren, X., Lauro, S.E., Soldovieri, F., Zeng, X., Gao, X., Chen, W., Dai, S., Liu, D., Zhang, G., Zuo, W., Wen, W., Zhang, Z., Zhang, X., Zhang, H., 2020. The Moon's farside shallow subsurface structure unveiled by Chang'E-4 lunar penetrating radar. Sci. Adv. 6 (9) https://doi.org/10.1126/sciadv.aay6898 eaay6898.

Lin, H., He, Z., Yang, W., Lin, Y., Xu, R., Zhang, C., Zhu, M.-H., Chang, R., Zhang, J., Li, C., Lin, H., Liu, Y., Gou, S., Wei, Y., Hu, S., Xue, C., Yang, J., Zhong, J., Fu, X., Wan, W., Zou, Y., 2019. Olivine-norite rock detected by the lunar rover Yutu-2 likely crystallized from the SPA impact melt pool. Natl. Sci. Rev. https://doi.org/10.1093/nsr/nwz183 nwz183.

Ling, Z., Qiao, L., Liu, C., Cao, H., Bi, X., Lu, X., Zhang, J., Fu, X., Li, B., Liu, J., 2019. Composition, mineralogy and chronology of mare basalts and non-mare materials in Von Kármán crater: landing site of the Chang'E-4 mission. Planet. Space Sci. 179, 104741. https://doi.org/10.1016/j.pss.2019.104741.

Lu, Y., Wu, Y., Michael, G.G., Ma, J., Cai, W., Qin, N., 2021. Chronological sequence of Chang'E-4 landing zone within Von Kármán crater. Icarus 354. https://doi.org/10.1016/j.icarus.2020.114086.

Lucey, P.G., Korotev, R.L., Gillis, J.J., Taylor, L.A., Lawrence, D., Campbell, B.A., Elphic, R., Feldman, B., Hood, L.L., Hunten, D., Mendillo, M., Noble, S., Papike, J.J., Reedy, R.C., Lawson, S., Prettyman, T., Gasnault, O., Maurice, S., 2006. Understanding the lunar surface and space-moon interactions. In: Jolliff, B., Wieczorek, M., Shearer, C., Neal, C.R. (Eds.), New Views of the Moon. Mineralogical Society of America, Chantilly, Virginia, pp. 83–220. https://doi.org/10.2138/rmg.2006.60.2.

McGetchin, T.R., Settle, M., Head, J.W., 1973. Radial thickness variation in impact crater ejecta: implications for lunar basin deposits. Earth Planet. Sci. Lett. 20 (2), 226–236. https://doi.org/10.1016/0012-821X(73)90162-3.

Melosh, H.J., 1989. Impact Cratering: A Geologic Process. Oxford University Press New York.

Moriarty, D.P., Pieters, C.M., 2018. The character of south pole - Aitken basin: patterns of surface and sub-surface composition. J. Geophys. Res. Planet. 123 (3), 729–747. https://doi.org/10.1002/2017JE005364.

Neal, C.R., Taylor, L.A., 1992. Petrogenesis of mare basalts: a record of lunar volcanism. Geochim. Cosmochim. Acta 56 (6), 2177–2211. https://doi.org/10.1016/0016-7037(92)90184-K.

Nelson, D.M., Koeber, S.D., Daud, K., Robinson, M.S., Watters, T.R., Banks, M.E., Williams, N.R., 2014. Mapping lunar maria extents and lobate scarps using LROC image products. In: The 45th Lunar and Planetary Science Conference (#2861).

Oberbeck, V.R., Hörz, F., Morrison, R.H., Quaide, W.L., Gault, D.E., 1975. On the origin of the lunar smooth-plains. Moon 12 (1), 19–54.

Orgel, C., Michael, G., Fassett, C.I., van der Bogert, C.H., Riedel, C., Kneissl, T., Hiesinger, H., 2018. Ancient bombardment of the inner solar system: reinvestigation of the "fingerprints" of different impactor populations on the lunar surface. J. Geophys. Res. Planet. 123 (3), 748–762. https://doi.org/10.1002/2017je005451.

Otake, H., Ohtake, M., Hirata, N., 2012. Lunar iron and titanium abundance algorithms based on SELENE (Kaguya) Multiband Imager data. In: The 43rd Lunar and Planetary Science Conference (#1905).

Pike, R.J., 1974. Ejecta from large craters on the moon: comments on the geometric model of McGetchin et al. Earth Planet. Sci. Lett. 23 (3), 265–271. https://doi.org/10.1016/0012-821X(74)90114-9.

Prettyman, T.H., Hagerty, J.J., Elphic, R.C., Feldman, W.C., Lawrence, D.J., McKinney, G.W., Vaniman, D.T., 2006. Elemental composition of the lunar surface: analysis of gamma ray spectroscopy data from lunar prospector. J. Geophys. Res. Planet. 111, E12007 https://doi.org/10.1029/2005je002656.

Schultz, P.H., Spudis, P.D., 1979. Evidence for ancient mare volcanism. In: The 10th Lunar and Planetary Science Conference, pp. 2899–2918.

Shawe-Taylor, J., Cristianini, N., 2004. Kernel Methods for Pattern Analysis. Cambridge University Press.

Tobler, W.R., 1970. A computer movie simulating urban growth in the Detroit region. Econ. Geogr. 46 (sup1), 234–240. https://doi.org/10.2307/143141.

Uemoto, K., Ohtake, M., Haruyama, J., Matsunaga, T., Yamamoto, S., Nakamura, R., Yokota, Y., Ishihara, Y., Iwata, T., 2017. Evidence of impact melt sheet differentiation of the lunar south pole-Aitken basin. J. Geophys. Res. Planet. 122, 1672–1686. https://doi.org/10.1002/2016JE005209.

Vaughan, W.M., Head, J.W., 2014. Impact melt differentiation in the south pole-Aitken basin: some observations and speculations. Planet. Space Sci. 91, 101–106. https://doi.org/10.1016/j.pss.2013.11.010.

Whitten, J., Head, J.W., 2015a. Lunar cryptomaria: mineralogy and composition of ancient volcanic deposits. Planet. Space Sci. 106, 67–81. https://doi.org/10.1016/j.pss.2014.11.027.

Whitten, J.L., Head, J.W., 2015b. Lunar cryptomaria: physical characteristics, distribution, and implications for ancient volcanism. Icarus 247, 150–171. https://doi.org/10.1016/j.icarus.2014.09.031.

Wieczorek, M.A., Zuber, M.T., 2001. A Serenitatis origin for the Imbrian grooves and south pole-Aitken thorium anomaly. J. Geophys. Res. 106 (E11), 27853–27864. https://doi.org/10.1029/2000je001384.

Wieczorek, M.A., Neumann, G.A., Nimmo, F., Kiefer, W.S., Taylor, G.J., Melosh, H.J., Phillips, R.J., Solomon, S.C., Andrews-Hanna, J.C., Asmar, S.W., Konopliv, A.S., Lemoine, F.G., Smith, D.E., Watkins, M.M., Williams, J.G., Zuber, M.T., 2013. The crust of the moon as seen by GRAIL. Science 339 (6120), 671–675. https://doi.org/10.1126/science.1231530.

Xie, M., Liu, T., Xu, A., 2020. Ballistic sedimentation of impact crater ejecta: implications for the provenance of lunar samples and the resurfacing effect of ejecta on the lunar surface. J. Geophys. Res. Planet. 125 (5) https://doi.org/10.1029/2019je006113.